Draft version September 4, 2014
Preprint typeset using LaTeX style emulateapj v. 11/10/09

arXiv:1409.0861v1 [astro-ph.SR] 2 Sep 2014

CO/H_2 ABUNDANCE RATIO $\approx 10^{-4}$ IN A PROTOPLANETARY DISK*

Kevin France[1], Gregory J. Herczeg[2], Matthew McJunkin[1], Steven V. Penton[3]

Draft version September 4, 2014

ABSTRACT

The relative abundances of atomic and molecular species in planet-forming disks around young stars provide important constraints on photochemical disk models and provide a baseline for calculating disk masses from measurements of trace species. A knowledge of absolute abundances, those relative to molecular hydrogen (H_2), are challenging because of the weak rovibrational transition ladder of H_2 and the inability to spatially resolve different emission components within the circumstellar environment. To address both of these issues, we present new contemporaneous measurements of CO and H_2 absorption through the "warm molecular layer" of the protoplanetary disk around the Classical T Tauri Star RW Aurigae A. We use a newly commissioned observing mode of the *Hubble Space Telescope*-Cosmic Origins Spectrograph to detect warm H_2 absorption in this region for the first time. An analysis of the emission and absorption spectrum of RW Aur shows components from the accretion region near the stellar photosphere, the molecular disk, and several outflow components. The warm H_2 and CO absorption lines are consistent with a disk origin. We model the 1092 – 1117 Å spectrum of RW Aur to derive $\log_{10}$ N(H_2) = $19.90^{+0.33}_{-0.22}$ cm^{-2} at $T_{rot}(H_2)$ = 440 ± 39 K. The CO $A-X$ bands observed from 1410 – 1520 Å are best fit by $\log_{10}$ N(CO) = $16.1\ ^{+0.3}_{-0.5}$ cm^{-2} at T_{rot}(CO) = 200^{+650}_{-125} K. Combining direct measurements of the H I, H_2, and CO column densities, we find a molecular fraction in the warm disk surface of $f_{H2} \geq 0.47$ and derive a molecular abundance ratio of CO/H_2 = $1.6^{+4.7}_{-1.3} \times 10^{-4}$, both consistent with canonical interstellar dense cloud values.

Subject headings: protoplanetary disks — stars: individual (RW Aur A) — ultraviolet: planetary systems

1. INTRODUCTION

The gas and dust in protostellar disks provide the raw materials for planet building. The formation of giant planet cores through the coagulation of dust grains (Hayashi et al. 1985) is thought to be complete prior to the 2 – 4 Myr dust disk clearing timescale (Hernández et al. 2007; Ingleby et al. 2011a; Fang et al. 2013). The majority of giant planet formation is thought to take place inside of $\sim$ 10 AU (Mordasini et al. 2009), and these protoplanets accrete their outer layers and atmospheres from the protoplanetary gas disk prior to its dissipation (Ida & Lin 2004). The final mass and composition of protoplanets are therefore closely related to the abundances, spatial distributions, and lifetimes of the gas in the circumstellar environment. The gas disk also regulates planetary migration (Ward 1997; Armitage et al. 2002; Trilling et al. 2002); the migration timescale is sensitive to the specifics of the disk surface density distribution and lifetime (Armitage 2007). Gas disk dissipation timescales inferred from accretion indicators are found to be similar to the dust-clearing timescale ($\approx$ 2 – 5 Myr; Fedele et al. 2010; Jayawardhana et al. 2006; Sicilia-Aguilar et al. 2005). However, direct gas disk observations indicate that inner molecular disks can persist to ages $\gtrsim$ 10 Myr in some Classical T Tauri Stars (CTTSs) and transitional systems (see, e.g., the review presented in Najita et al. 2007; Salyk et al. 2009; Ingleby et al. 2011a; France et al. 2012b), although these results are based on a relatively small number of protoplanetary systems.

The composition of a planetary system is also impacted by the initial abundances in the protoplanetary environment, in particular the C/O ratio (Bond et al. 2010; Öberg et al. 2011). Observations and models of the atomic and molecular composition of young circumstellar disks are useful tools for creating an inventory of the materials available for planet formation (e.g., Aikawa et al. 1997; Thi et al. 2004), as well as providing constraints on photochemical models of the protoplanetary environment (Dullemond et al. 2007; Visser et al. 2011). An unexpected observational discovery from the *Hubble Space Telescope*-Cosmic Origins Spectrograph (COS) was the detection and characterization of carbon monoxide (CO) in the far-ultraviolet (far-UV; $1150 \leq \lambda \leq 1750$ Å) spectra of low-mass protoplanetary systems. France et al. (2011a) presented the first detections of far-UV emission and absorption lines of CO in these environments. It was shown that these CO lines provide unique diagnostics of the disk structure and that the strength of these features is surprising in light of the expected abundance of CO in the disk. Models of the CO and H_2 emission indicated that the observed CO/H_2 ratio ($\equiv N(CO)/N(H_2)$)

* Based on observations made with the NASA/ESA *Hubble Space Telescope*, obtained from the data archive at the Space Telescope Science Institute. STScI is operated by the Association of Universities for Research in Astronomy, Inc. under NASA contract NAS 5-26555.

[1] Center for Astrophysics and Space Astronomy, University of Colorado, 389 UCB, Boulder, CO 80309; kevin.france@colorado.edu
[2] Kavli Institute for Astronomy and Astrophysics, Peking University, Beijing 100871, China
[3] Space Telescope Science Institute, 3700 San Martin Drive, Baltimore MD, 21218, USA

was in the range $0.1 \leq CO/H_2 \leq 1$ (France et al. 2011a; Schindhelm et al. 2012a).

Initial CO and H_2 absorption line measurements in CTTSs indicated similarly high CO/H_2 ratios. France et al. (2012a) presented an analysis of the molecules on a sightline through the AA Tauri circumstellar disk, observing CO against the far-UV continuum and H_2 absorption against the broad Lyα line that originates in the protostellar atmosphere (see also Yang et al. 2011). In agreement with the emission line work, they find $CO/H_2 \approx 0.4$, providing an independent measure of large CO abundance ratios in protoplanetary environments.

The large abundances of CO are surprising because protoplanetary disks form in dense clouds, where the CO/H_2 ratio is usually assumed to be $\sim 10^{-4}$ (Lacy et al. 1994). Furthermore, recent work on the gas composition at larger disk radii suggests a depleted CO/H_2 ratio (Bergin et al. 2013; Favre et al. 2013). These results raise questions about the mass budget and chemical composition of the gas phase at planet-forming radii ($a < 10$ AU). Do the UV data imply that the local CO/H_2 abundance ratio of order unity, or is this result biased by spatial stratification of the emitting/absorbing molecular populations? Because we expect H_2 to be abundant in almost all regions of the protoplanetary gas disk, is there a particular spatial or temperature structure that makes the majority of the warm H_2 hard to detect? From an observational perspective, the question is: where is the H_2 that should be associated with the large reservoir of CO observed in the UV spectra?

1.1. *CO/H_2 at Planet-forming Radii, Where is the Warm H_2?*

Despite considerable observational effort dedicated to the characterization of warm H_2 ($T_{rot}(H_2) \sim 500$ K) in CTTS environments, the rovibrational emission lines have proven challenging to characterize in sources without strong outflows (e.g., Beck et al. 2008). The homonuclear nature of H_2 means that rovibrational transitions are dipole forbidden, with weak quadrupole transitions that have large energy spacing. This makes direct detection of H_2 challenging at near- and mid-IR wavelengths (Pascucci et al. 2006; Lahuis et al. 2007; Bitner et al. 2008; but see also Bary et al. 2008), and dedicated searches have usually returned upper limits (e.g., Carmona et al. 2008; Martin-Zaïdi et al. 2010) or tentative detections around more massive Herbig Ae star disks (Richter et al. 2002).

The observational results described above are roughly consistent with disk models that find a significant CO population in the disk surface near $N_H \sim 10^{21}$ cm^{-2} where the hydrogen molecular fraction is low (e.g., Glassgold et al. 2004); in this case the regions of high local CO/H_2 ratio may be limited to narrow layers in the upper disk atmosphere where far-UV H_2 fluorescence originates, and not representative of the warm molecular disk as a whole. A key difference between the CO and H_2 populations observed in UV spectra is the derived rotational temperature: CO emission/absorption originates in a warm ($T_{rot}(CO) \sim 300$ – 700 K, $N(CO) \sim 10^{17-19}$ cm^{-2}) molecular gas while the H_2 emission/absorption comes from a hotter ($T_{rot}(H_2) \sim 2000$ – 3000 K, $N(H_2) \sim 10^{18-19}$ cm^{-2}) molecular phase (Herczeg et al. 2004; Schindhelm et al. 2012a). One interpretation is that the previous UV observations probe CO at large semi-major axes ($a \gtrsim 2$AU), and that this gas is spatially distinct from the hot H_2-emitting gas orbiting at terrestrial planet radii ($0.1 < a \lesssim 2$ AU). This interpretation is supported by an analysis of the emission line-widths. Assuming that Keplerian rotation dominates the observed velocity broadening, the narrower spectral lines of the warm CO suggest an origin at larger disk radii than the hot H_2 (Schindhelm et al. 2012a; France et al. 2012b). Alternatively, if the line-broadening is not dominated by rotation and non-thermal processes control the molecular level populations, then the rotational temperature may not reflect the local kinetic temperature of the molecular gas (France et al. 2012a). In this case, the observed CO and H_2 may be approximately co-spatial with a very large CO abundance.

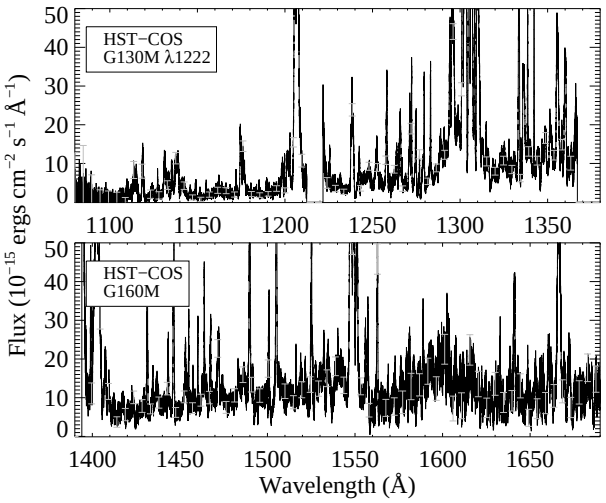

FIG. 1.— Overview of the 29 August 2013 *HST*-COS observations of RW Aur A. The data are displayed as the black histogram with representative error bars shown in gray.

The combination of CO and H_2 fluorescence observations and emission line modeling have raised intriguing questions regarding the composition and spatial distribution of the molecular material at planet-forming radii, however, absorption spectroscopy provides the most direct, model-independent means of measuring the column densities on the line-of-sight through these disks. An analysis of 34 T Tauri stars found a roughly 25% detection rate of warm CO absorption similar to AA Tau in gas-rich disks (McJunkin et al. 2013). The McJunkin study identified six moderate-inclination disks with $T_{rot}(CO) \sim 500$ K CO absorption. These targets spanned a range of stellar masses (~ 0.4 – 2.3 $M_\odot$), ages (~ 0.6 – 6 Myr), and mass accretion rates ($(0.1 - 3) \times 10^{-8}$ $M_\odot$ yr^{-1}). While H_2 absorption spectroscopy has been carried out for the intrinsically hotter and brighter Herbig stars (Roberge et al. 2001; Martin-Zaïdi et al. 2008) by the *Far-Ultraviolet Spectroscopic Explorer* (*FUSE*), lower-luminosity CTTSs do not produce sufficient flux to be used as a background source for disk absorption studies with *FUSE*.

The McJunkin et al. sample took advantage of the increased sensitivity of the *HST*-COS to provide a tar-

get list of protoplanetary disks with known molecular absorbers, but relatively low reddening. Unfortunately, the "traditional" *HST* far-UV bandpass (1150 – 1750 Å) does not provide spectral coverage of H_2 gas with kinetic temperatures of a few hundred degrees. Thermal excitation at 300 – 700 K will produce an appreciable population of H_2 in the $v = 0$, $J'' = 0 - 5$ levels, whose transitions reside at $\lambda < 1126$ Å (the longest wavelength transition for H_2 in $J'' = 5$ is the Lyman (0 – 0) P(5) line at 1125.54 Å). Spectral coverage in the $1090 \lesssim \lambda \lesssim 1130$ Å wavelength region is required to measure both the column density and kinetic temperature of the warm H_2 disk.

During on-orbit verification following *HST* Servicing Mission-4, it was demonstrated that *HST* + COS maintains spectroscopic sensitivity down to the Lyman edge at 912 Å (McCandliss et al. 2010). We take advantage of this short-wavelength response, in combination with a new medium resolution mode of COS developed in part for this work, to directly measure the CO/H_2 column density ratio in the warm molecular phase of a CTTS disk, RW Aur A (Section 2), for the first time. In Section 3, we describe the new G130M λ1222 mode used for these observations of the disk around RW Aur A and the data analysis used to extract H_2 and CO absorption line profiles from the data. In Section 4, we describe the CO and H_2 modeling analyses used to derive column densities and excitation temperatures in RW Aur A, and demonstrate that this line-of-sight absorption originates in the circumstellar environment. Section 5 presents an analysis of the velocity fields present in RW Aur A, showing that the molecular disk component can be readily separated from the molecular and atomic outflows. We conclude Section 5 with a discussion of the CO/H_2 ratio and present a brief summary in Section 6.

2. RW AURIGAE

The RW Aur system is composed of two pre-main-sequence K stars, separated by approximately 1.5″ (Duchêne et al. 1999), at a distance from Earth of $d \approx 140$ pc (Elias 1978; Kenyon & Hartmann 1995; Torres et al. 2007). The primary component (RW Aur A) is likely a K0 – K4 star ($M_\star \approx 1.1 - 1.4$ $M_\odot$; see Woitas et al. 2001 and references therein), roughly 30 – 50% more massive than the K5 – K7 B component (Herczeg & Hillenbrand 2014). RW Aur A displays a near-infrared (near-IR) excess indicative of a warm inner dust disk (Hartigan et al. 1995) and a total disk mass (assuming a gas-to-dust ratio of 100) $\sim 4 \times 10^{-3}$ $M_\odot$ (Andrews & Williams 2005).

Disk inclination estimates range from 45° – 90°, with sub-mm maps favoring lower inclinations (Cabrit et al. 2006) and near-IR interferometry suggesting higher values (Eisner et al. 2007). Cabrit et al. (2006) describe high-resolution single-dish interferometric measurements of the millimeter dust continuum and CO rotational lines. Modeling these data as a Keplerian disk rotating about the jet-axis of the system (see below), they find best-fit outer disk inclinations ranging from 45 – 60°, depending on assumptions about jet structure and velocity. Eisner et al. (2007) describe multiple epochs of near-IR spectroscopy and interferometry to constrain the size, luminosity, variability and inclination of the *inner* disk ($r < 2$ AU) around RW Aur A. Their observations and subsequent uniform disk modeling find $i = 77^{\circ}{}^{+13}_{-15}$.

CO fundamental emission lines observed at NIRSPEC (Najita et al. 2003) suggest a double-peaked emitting structure, with a best-fit disk inclination of $i = 60°$. However, these observations and higher-resolution spectra from CRIRES (Brown et al. 2013) show that the broad CO lines are severely blended and may include a contribution from a molecular wind, complicating the estimation of Keplerian disk parameters from these data. The 4.7 μm CO data only show CO emission, with no central reversal as is observed in some CTTS and Herbig spectra (Brown et al. 2013). McJunkin et al. (2013) combined simple disk structure models with the first epoch of *HST*-COS CO absorption line data (described above) to determine that the $A - X$ absorption lines originate above the $A_V = 1$ dust surface, finding that for dimensionless disk height $z/r = 0.6$, the RW Aur disk must have inclination $> 60°$ to account for the observed absorption. In the subsequent sections, we will argue that the majority of the absorbing molecular gas that we observe in the RW Aur A system comes from a warm inner region. Evaluating the various inclination estimates, we conclude that the inner disk inclination of RW Aur A is $i \geq 60°$.

Using a combination of ground-based optical spectra, *HST* near-UV spectra, and accretion shock models, Ingleby et al. (2013) find a mass accretion rate of 2.0×10^{-8} $M_\odot$ yr^{-1} for RW Aur A. The more massive A component appears to have a higher mass accretion rate (Hartigan et al. 1995; White & Ghez 2001) and therefore should dominate the far-UV accretion luminosity that creates the background flux for the disk absorption line spectroscopy studied here. Furthermore, the *HST*-COS instrumental response falls off sharply at $\theta > 0.5''$ from the center of the primary science aperture, and we conclude that RW Aur B does not contribute significantly to the observed far-UV flux. The optical extinction towards RW Aur A is not well constrained due to heavy veiling, but the optical extinction towards RW Aur B ($A_V = 0.10$; Herczeg & Hillenbrand 2014) is very similar to the value found from interstellar Lyα absorption ($\log_{10}$ N(HI) $= 20.25^{+0.05}_{-0.21}$ cm^{-2}) towards RW Aur A, assuming standard ISM gas-to-dust conversions ($A_V = 0.11$; McJunkin et al. 2014).

RW Aur A has a well-studied bipolar outflow, with the redshifted component ($v_{red} \sim +100$ km s^{-1}) having higher density and surface brightness than the blueshifted component (Hirth et al. 1994; Melnikov et al. 2009). The far-UV spectrum of RW Aur A has been studied in detail in two recent papers, one focusing on hot gas emission originating near the stellar surface (Ardila et al. 2013) and one studying H_2 emission from the disk and outflow (France et al. 2012b). RW Aur showed the highest velocity molecular outflow emission in the France et al. (2012b) survey, with both redshifted and blueshifted emission observed in the strong H_2 fluorescence lines excited by Lyα photons produced in the outflow/jet, reminiscent of the spatially-resolved T Tau molecular outflow (Walter et al. 2003). The UV H_2 emission peaks 80 – 110 km s^{-1} to the red of the stellar velocity, suggesting that the molecular emission arises in material that is approximately

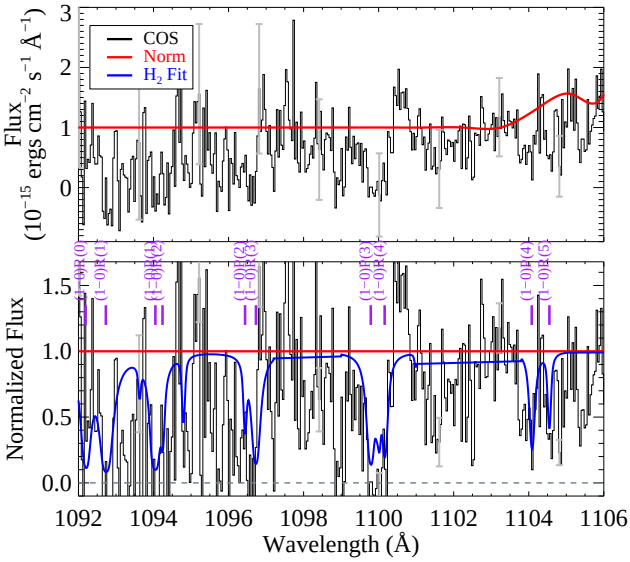

FIG. 2.— *HST*-COS spectra of the 1092 – 1106 Å spectral region, with the continuum function shown as the solid red line (top panel). The bottom panel shows the normalized flux and the best-fit H_2 absorption model as the blue solid line (§4.1). The strongest H_2 absorption lines with $J'' \leq 5$ are labeled in purple. The data and the normalized spectra are binned by 4 pixels and smoothed with a 3 pixel boxcar average for display. The normalized spectra are smoothed with a 3 pixel boxcar average prior to H_2 fitting.

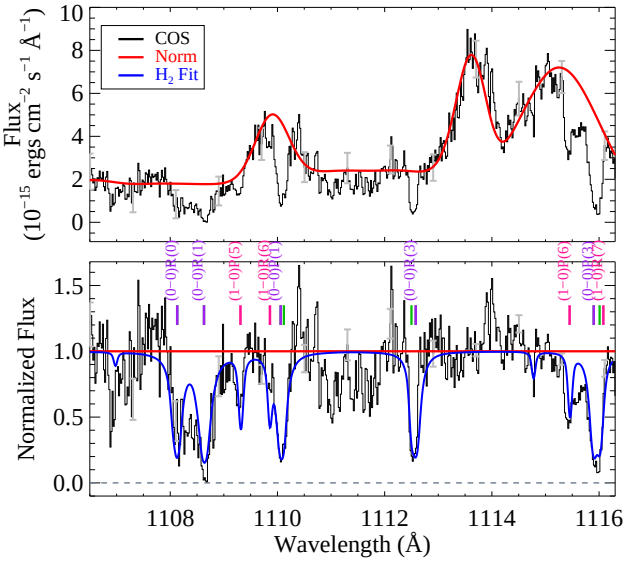

FIG. 3.— *HST*-COS spectra of the 1106 – 1116.5 Å spectral region, with the continuum function shown as the solid red line (top panel). The large emission features in the red spectrum are H_2 fluorescent emission lines, approximated by Gaussians for the purpose of constructing the normalization curve. The bottom panel shows the normalized flux and the best-fit H_2 absorption model as the blue solid line (§4.1). The data and the normalized spectra are binned by 2 pixels and smoothed with a 3 pixel boxcar average for display. The normalized spectra are smoothed with a 3 pixel boxcar average prior to H_2 fitting. The best-fit H_2 absorption model is parameterized with $N(H_2) = 19.90^{+0.33}_{-0.22}$ cm^{-2}, $b_{H2} = 4 \pm 1$ km s^{-1}, a radial velocity $v_{H2abs} = 5 \pm 5$ km s^{-1} and a covering fraction $f_{cov}^{H2} = 0.974 \pm 0.027$. Transitions to $v' = 0$ are labeled in purple and transitions to $v' = 1$ are labeled in pink. For display clarity, we have omitted labels from close blends, noting them with a green tick. The unlabeled lines are: (0 – 0) R(2) 1110.12 Å, (0 – 0) P(2) 1112.50 Å, and (0 – 0) R(4) 1116.01 Å.

cospatial with the forbidden atomic line (e.g., [S II] λ6731) emission (Woitas et al. 2002; Melnikov et al. 2009; Hartigan & Hillenbrand 2009). The near-IR H_2 outflow from RW Aur is centered near +44 km s^{-1} (Beck et al. 2008), significantly bluer than the peak of the far-UV H_2 velocity profile. We will return to the velocity structure of the far-UV spectrum in Section 5.1.

3. OBSERVATIONS AND DATA REDUCTION: DIRECT MEASUREMENT OF WARM CIRCUMSTELLAR H_2 AT $\lambda < 1120$ Å WITH *HST*-COS

The G130M λ1222 mode on COS, introduced for *HST* Cycle 20 observations, has made possible high-sensitivity, moderate-resolution ($R \geq 10^4$; $\Delta\lambda \leq 0.1$ Å) spectroscopy in the 1064 – 1130 Å bandpass from *HST* for the first time, delivering ≈ 15× the effective area of *FUSE* at 1110 Å. The `CENWAVE` λ1222 mode is chosen by moving the angle and focus position of the G130M grating to a setting that is considerably beyond the original G130M default locations (Penton et al. 2012, 2013). The COS "optics select mechanism 1" is rotated ≈ 0.8° and the grating focus mechanism is moved by ≈ 0.78 mm past the default (`CENWAVE` λ1291) range. This setting allows COS observations over the spectral range 1064 – 1214 Å on the FUV "B' segment, and 1223 - 1368 Å on the FUV "A" segment. This configuration intentionally places geocoronal Lyα on the small gap between the detector segments to minimize microchannel plate gain sag. The instrument focus in the λ1222 setting is chosen to optimize resolution on the FUV B-segment.

The observations presented here are the first science observations collected with the G130M λ1222 mode, obtained as part of the *Warm H_2 In Protoplanetary Systems* (WH_2IPS) Cycle 20 *HST* Guest Observing program (PID 12876). The WH_2IPS observing strategy is to combine long exposure times (several orbits) at the short wavelength end of the COS bandpass to measure lines from the H_2 (1 – 0) $\lambda_o \sim 1092$ Å and (0 – 0) $\lambda_o \sim 1108$ Å Lyman band systems with shorter observations with the G160M grating (1400 – 1750 Å) to contemporaneously observe the CO $A - X$ electronic absorptions into the $0 \leq v' \leq 4$ vibrational bands. The CO absorption spectrum along the RW Aur A sightline was analyzed by McJunkin et al. (2013), however the system geometry and accretion rates of CTTS systems are time-variable, so we re-observed the CO spectra to be directly comparable with our new H_2 absorption line measurements.

We observed RW Aur A (05^h 07^m 49.58^s +30° 24′ 04.9″) with *HST*-COS on 29 August 2013. We employed the G130M λ1222 mode for a total of 10468s (4 orbits) in all four focal-plane split positions (Green et al. 2012). We observed with the longer-wavelength G160M mode in four central wavelength settings, each with a different focal-plane position for a total of 5613s (2 orbits). The use of multiple focal-plane positions allows for continuous wavelength coverage while minimizing the impact of fixed-pattern noise. We coadded the spectra using a modified version of the IDL-based COS far-UV data reduction routines first described by Danforth et al. (2010). The data, displayed in Figure 1, have a spectral resolving power of $R \approx 16000$ ($\Delta v = 19$ km s^{-1}) at

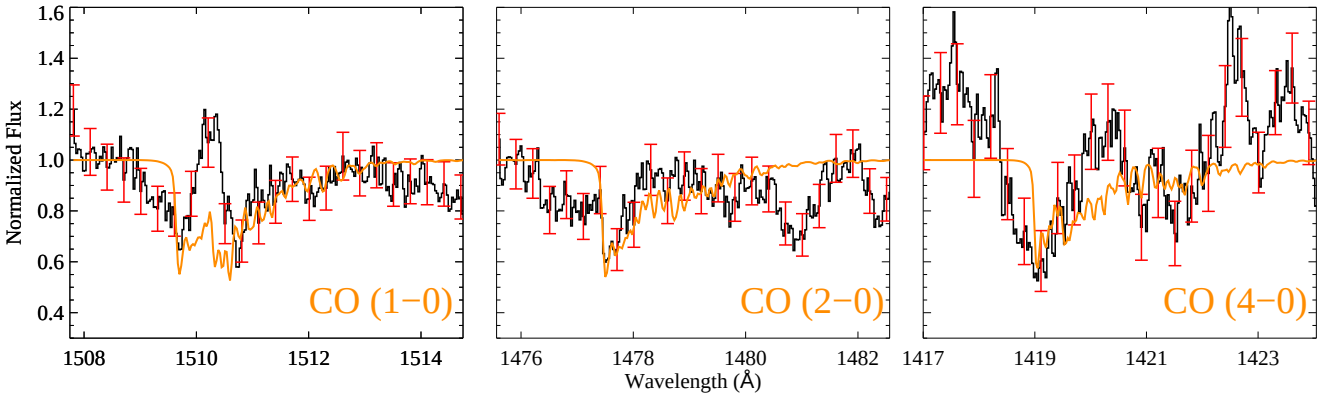

FIG. 4.— CO ($A-X$) absorption spectra for $v^{'}=1$, 2, and 4. The data are normalized to the local continuum level around each band, and the best-fit model spectrum is shown in orange. Contamination by H_2 emission lines compromise continuum and absorption band determination and drive the uncertainty on the best-fit CO absorption model, parameterized with $N(\mathrm{CO}) = 16.1^{+0.3}_{-0.5}$ cm^{-2}, $T_{rot}(\mathrm{CO}) = 200^{+650}_{-125}$, $b_{CO} = 0.5 \pm 0.1$ km s^{-1}, and $v_{COabs} \approx 5 \pm 5$ km s^{-1}.

1110 Å and $R \approx 18000$ ($\Delta v = 17$ km s^{-1}) at 1600 Å. The absolute velocity accuracy of these modes is ≈ 15 km s^{-1}.

The primary scientific focus of this work is the quantitative treatment of the molecular lines observed in absorption against the far-UV continuum from RW Aur A. The far-UV continuum in CTTSs is a superposition of a molecular quasi-continuum ($1400 \lesssim \lambda \lesssim 1660$ Å) and a component that can be well-represented by a linear or quadratic function (France et al. 2011b). The linear continuum is well-correlated with accretion indicators such as C IV line flux, however appears distinct from the well-studied near-UV Balmer continuum (France et al. 2014). In any case, the far-UV continuum is smoothly varying on spectral scales of ~ 10 Å, and we assume the local continua have a linear shape for the purposes of continuum normalization (Figure 2).

Because the COS observations are spatially unresolved, we are observing the entire star-disk system simultaneously. As such there are many fluorescent H_2 emission lines that contaminate the fitting regions. In the region of the H_2 $B^1\Sigma_u^+ - X^1\Sigma_g^+$ (0 – 0) band between 1108 – 1116 Å, there are several blended H_2 emission lines upon which we observe the H_2 absorption (Figure 3). We normalize these spectra by assuming that the underlying spectrum can be parameterized with a combination of linear continuum and Gaussian emission lines, as shown in Figure 3. For the case of the CO absorption spectra in the G160M band (Figure 4), the emission lines are typically narrow and we simply exclude these regions when computing the best-fit CO parameters.

4. COLUMN DENSITY AND TEMPERATURE ANALYSIS

4.1. *H_2 Fitting*

In order to assess the CO/H_2 abundance ratio in the RW Aur disk, as well as determine the co-spatiality of the absorbing gas, the column densities, rotational temperatures, and velocity structures must be derived from the spectra. The H_2 absorption lines were fitted with an IDL-based routine that combines the *H_2ools* optical depth templates (McCandliss 2003) and the MPFIT least-squares minimization routines (Markwardt 2009). The column densities of each rotational level $J^{''}$ in the ground electrovibrational level, $N(\mathrm{H_2}[v^{''}=0, J^{''}])$ (in units of cm^{-2}), are allowed to vary simultaneously. The first 9 rotational levels are considered ($J^{''} = 0-8$); lines originating in $J^{''} \geq 9$ were not detected. The Doppler b-value ($b_{H2} = (2kT_{rot}(\mathrm{H_2})/\mathrm{m}_{H2} + v_{turb}^2)^{1/2}$, in units of km s^{-1}), the radial velocity of the absorption lines (in units of km s^{-1}), and the molecular gas covering fraction are also free parameters in the fit. The normalized spectra (Figures 2 and 3) are smoothed with a 3 pixel boxcar average prior to H_2 fitting. A synthetic normalized absorption spectrum is created for each combination of free parameters and this theoretical spectrum is convolved with the COS line-spread-function[5] (Kriss 2011). The process iterates until the best-fit parameters are found.

Systematic uncertainties on the continuum normalization are explicitly taken into account during the fitting, and we execute an independent test to assess the magnitude of systematic uncertainties. We vary parameters on the continuum normalization function until it deviates beyond the 1-sigma photometric error bars on the data. The best-fit H_2 parameters are then re-derived and the difference between these and the nominal best-fit parameters are taken as the systematic errors.

The spectral model comparison was carried out over the 1092.5 – 1117 Å spectral window that covers most of the Lyman band absorptions from the (1 – 0) and (0 – 0) systems. The individual best-fit column densities and statistical errors are shown in Table 1. Spectral blending with $J^{''}=3$ states makes the column densities for $J^{''}=2$ and $J^{''}=7$ unreliable; the $J^{''}=3$ lines are reasonably well-constrained from the (1 – 0) band alone therefore these states are more robustly determined and dominate the fits in the 1106 – 1117 Å region. Consequently, we do not incorporate the $J^{''}=2$ and 7 lines in the subsequent analysis[6]. The best-fit H_2 model spectrum is displayed

[5] The COS LSF experiences a wavelength dependent non-Gaussianity due to the introduction of mid-frequency wave-front errors produced by the polishing errors on the *HST* primary and secondary mirrors; `http://www.stsci.edu/hst/cos/documents/isrs/`

[6] including the $J^{''}=2$ and 7 column densities in the rotational temperature fit reduces the rotational temperature by $\lesssim 10$ %.

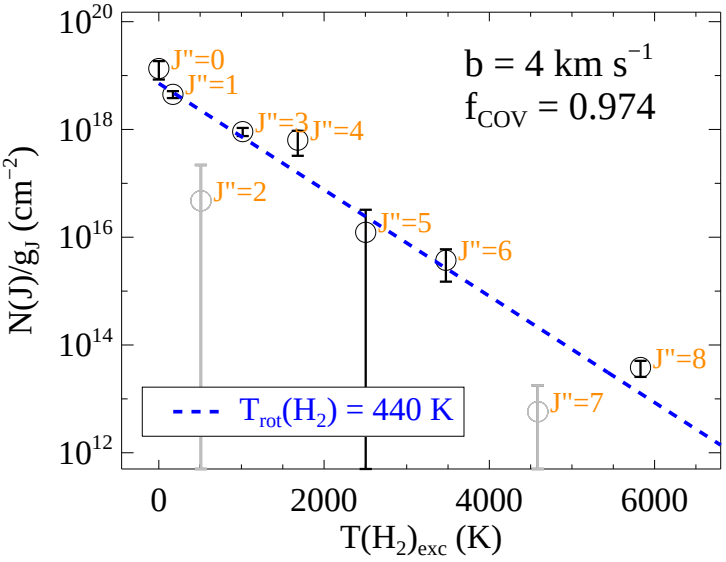

FIG. 5.— H_2 excitation diagram for the RW Aur disk absorption. As described in the text, $J^{''} = 2$ and 7 are poorly fit due to line blends and are not considered in the best fit excitation fit. We find a best-fit rotational excitation temperature of the H_2 of $T_{rot} = 440 \pm 39$ K.

TABLE 1
RW AUR A H_2 PARAMETERS[a].

H_2 Level	$\log_{10}$N(H_2, $v^{''} = 0$, $J^{''}$)
$J^{''} = 0$	19.13 ± 0.14
$J^{''} = 1$	19.61 ± 0.06
$J^{''} = 2$	...
$J^{''} = 3$	19.28 ± 0.07
$J^{''} = 4$	18.76 ± 0.17
$J^{''} = 5$	17.61 ± 0.42
$J^{''} = 6$	16.69 ± 0.20
$J^{''} = 7$	...
$J^{''} = 8$	14.81 ± 0.12
T_{rot}(H_2)	440 ± 39 K
b_{H2}	4 ± 1 km s^{-1}
f_{cov}^{H2}	0.974 ± 0.027

[a] Column densities in each ground rotational state, $J^{''}$, are in units of molecules cm^{-2}. Spectral fitting of $J^{''} = 2$ and 7 levels are compromised by spectral blending at the resolution and S/N of the COS data.

in blue in Figures 2 and 3. We find a total column of $\log_{10} N(H_2) = 19.90^{+0.33}_{-0.22}$ cm^{-2}. The uncertainty on the column density determination is a combination of statistical errors associated with the fitting process and systematic errors based on our choice of continuum normalization. These errors are distributed as ± 0.05 statistical fitting uncertainties and +0.33/−0.21 systematic uncertainties on the normalization. The model finds a best fit b-value of 4 ± 1 km s^{-1}, a radial velocity $v_{H2abs} = 5 \pm 5$ km s^{-1} and a covering fraction consistent with unity, $f_{cov}^{H2} = 0.974 \pm 0.027$.

The critical densities for the low-$J^{''}$ rotational levels of H_2 are $\lesssim 2 \times 10^4$ cm^{-3} (Mandy & Martin 1993). At the expected densities of the warm molecular disk layer ($n_{H2} \sim 10^6$; Woitke et al. 2009; Bruderer 2013) we expect the H_2 level populations to be determined by collisions. As such, the population will be described by the Maxwell-Boltzmann distribution with a form

$$N(J^{''})/N(J^{''} = 0) = \frac{g_{J^{''}}}{g_0} e^{(-E_{J^{''}}/kT_{rot})} \quad (1)$$

where T_{rot} is the rotational excitation temperature of the molecules, equal to the kinetic temperature ($T_{rot} = T_{kin}$) for a thermalized population. Figure 5 displays the H_2 excitation diagram for RW Aur A, from which a best fit $T_{rot}(H_2) = 440 \pm 39$ K is derived. Interestingly, a 440 K rotational temperature only corresponds to an H_2 thermal broadening of ≈ 2 km s^{-1}, suggesting that a turbulent velocity of $v_{turb} \sim 3 - 3.5$ km s^{-1} could be present. However, this result is somewhat speculative because the strongest absorption lines are damped and therefore not highly sensitive to the exact b-value. Higher S/N and spectral resolution measurements of H_2 absorption lines should be able to provide more direct constraints on the turbulent broadening in inner disks.

4.2. *CO Fitting*

The CO absorption line fitting and error estimation procedure is described in detail by McJunkin et al. (2013). We summarize it briefly for the reader here: We analyze three bands of the CO Fourth Positive ($A^1\Pi - X^1\Sigma^+$) system observed in our COS G160M spectra, (4 – 0), (2 – 0), and (1 – 0) with bandhead wavelengths of approximately 1419.0 Å, 1477.6 Å, and 1509.8 Å, respectively. Oscillator strengths and ground-state energy levels from the literature (Haridass & Huber 1994; Eidelsberg et al. 1999; Eidelsberg & Rostas 2003) are used to compute synthetic CO absorption spectra. We create a grid of model absorption spectra with the column densities of ^{12}CO and ^{13}CO ($N(^{12}$CO) and $N(^{13}$CO), in units of cm^{-2}), the CO rotational temperature T_{rot}(CO) (in units of Kelvin), the Doppler b-value (b_{CO}; in units of km s^{-1}), and the CO radial velocity (v_{COabs}; in units of km s^{-1}) as free parameters. This grid is compared against the normalized CO absorption spectra to determine the best-fit CO parameters. The ranges of our grid search were 0.1 – 2.0 km s^{-1} in steps of 0.1 km s^{-1} for the Doppler b-value, 100 - 1000 K with steps of 50 K for the rotational temperature, 14.0 - 18.0 in steps of 0.1 for $\log_{10}$(N(^{12}CO)), and 14.0 – 17.0 cm^{-2} in steps of 0.1 for $\log_{10}$(N(^{13}CO)). The maximum value of b_{CO} is limited by our assumptions that $v_{turb} < 1$ km s^{-1} and CO rotational temperatures $T_{rot}(CO) < 5 \times 10^3$ K.

The uncertainties on the model parameters were calculated from the photometric errors on the depth of the ^{12}CO bandhead in the observed COS spectra. The model parameter range was defined by varying each model parameter while keeping the other parameters constant; the best-fit parameter range was defined by models whose bandhead depths did not exceed the 1-sigma photometric error on the (2 – 0) bandhead depth in the data.

The best-fit CO parameters are $\log_{10}$ N(CO) = $16.1^{+0.3}_{-0.5}$ cm^{-2}, $T_{rot}(CO) = 200^{+650}_{-125}$ K, $b_{CO} = 0.5 \pm 0.1$ km s^{-1}, and $v_{COabs} = 5 \pm 5$

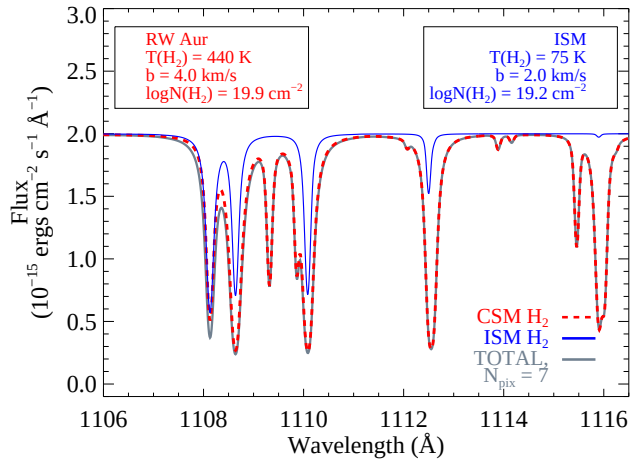

FIG. 6.— A comparison of model spectra for circumstellar H_2 (red dashed line) and interstellar H_2 (blue solid line) absorption systems shows that the circumstellar component dominates the total H_2 opacity. The interstellar absorption spectrum is calculated from the interstellar atomic hydrogen and dust reddening values for the RW Aur line-of-sight (McJunkin et al. 2014; §4.3).

km s^{-1}. These results are consistent with the CO absorption parameters determined for RW Aur previously (McJunkin et al. 2013). The normalized CO data with the best fit model are shown in Figure 4. We observe a possible blueshifted CO absorption component that may be associated with the low-ionization outflow, discussed in §5.1. The best fit ^{13}CO column density is $\log_{10}\ N^{13}(\mathrm{CO}) = 14.3$, however spectral blending with H_2 fluorescence lines and insufficient S/N prevent a meaningful determination of the $^{12}\mathrm{CO}/^{13}\mathrm{CO}$ ratio from these data.

4.3. *Circumstellar Origin of the H_2 Absorption*

There is a rich literature on interstellar H_2 and CO absorption line studies of the sightlines to hot stars, from early sounding rocket observations (Carruthers 1970), to *Copernicus* (Savage et al. 1977; Federman et al. 1980), though combined studies using *HST* and *FUSE* (Burgh et al. 2007; Sheffer et al. 2008). Therefore, it is important to demonstrate that the molecular absorption observed towards RW Aur is indeed circumstellar and not interstellar. This can be done with by comparing the properties of the H_2 and CO absorbers in RW Aur with those typical of the ISM.

The primary argument for the circumstellar origin of the observed H_2 is the observed rotational temperatures of the H_2 and CO populations. The average H_2 rotational (kinetic) temperature in the diffuse and translucent ISM is $\approx 60 - 100$ K (Savage et al. 1977; Rachford et al. 2002) and the CO temperatures (typically sub-thermal in the ISM) are < 10 K (Burgh et al. 2007; Sheffer et al. 2008). Therefore, the typical ISM temperatures of H_2 and CO are factors of ~ 6 and ~ 20 lower than observed for RW Aur, respectively. The molecular rotational temperatures derived from our COS spectra are instead consistent with those expected for a warm molecular layer of a protoplanetary disk atmosphere (Glassgold et al. 2004; Woitke et al. 2009; Meijerink et al. 2012).

The measured molecular column densities are also much larger than would be expected based on the interstellar reddening towards RW Aur. McJunkin et al. (2014) have recently presented direct measurements of the interstellar H I column densities towards a sample of 31 young stars, including RW Aur. For RW Aur, they measured $\log_{10}$ N(HI) $= 20.25^{+0.05}_{-0.21}$ cm^{-2} (the X-ray derived "H I column" is a factor of 10 higher, however, the X-ray absorption is not a direct measurement of the neutral hydrogen column, see McJunkin et al. 2014). Combining this with the well-characterized relationship between N(HI) and the selective reddening $E(B-V)$ (Diplas & Savage 1994)[7], we find $E(B-V) = 0.036$. The Bohlin et al. (1978) relation can then be used to calculate the expected interstellar H_2 column density: $2\mathrm{N}(\mathrm{H_2}) = (E(B-V) \times (5.8 \times 10^{21})$ - N(HI)). This yields an interstellar H_2 column density of $\log_{10}$ $\mathrm{N}_{ISM}(\mathrm{H_2}) = 19.19$ cm^{-2}, a factor of approximately 5 lower than observed towards RW Aur. This is shown graphically in Figure 6; we compare model absorption spectra of the ISM toward RW Aur (blue solid line) with the model fits to the observed data (red dashed line). As one can see, only in the (0 – 0) R(0) λ 1108.13 Å line does the ISM contribute appreciably to the opacity in the observed spectrum. The higher rotational states observed towards RW Aur are not predicted by the interstellar model.

An analogous argument can be made for the CO absorption lines. Burgh et al. (2007) show the CO column density as a function of $E(B-V)$ for interstellar sightlines (their Figure 3, *left*). For all sightlines with $E(B-V) < 0.2$, they find $\log_{10}$ $\mathrm{N}_{ISM}(\mathrm{CO}) \leq 13.3$. This is almost 10^3 times lower than the CO column density measured for RW Aur (§4.2). We conclude, based on both thermal and abundance arguments, that the H_2 and CO absorption line spectra observed towards RW Aur are completely dominated by circumstellar material.

5. DISCUSSION

5.1. *Spatially Decomposing the RW Aur A Environment: Velocity Fields*

As described in Section 2, the inner region of the RW Aur system is a dynamically active place. Material being funneled onto the central star, a rotating circumstellar disk, and atomic/molecular outflows are present within ~ 10 AU of the central star. In this subsection, we decompose the kinematic signatures of five individual velocity fields, and show that the H_2 and CO absorption described above most likely originate in the circumstellar disk orbiting RW Aur A. We show representative lines from all five velocity fields in Figure 7. A list of the observed spectral features in the COS spectra of RW Aur is presented in Table 2[8]. The absolute velocity accuracy of the COS FUV modes is ≈ 15 km s^{-1}.

5.1.1. *Molecular Disk*

The first velocity field comprises molecular emission and absorptions between ≈ -1 – $+15$ km s^{-1}, and we

[7] If we instead adopt the calibration of the N(HI) vs. $E(B-V)$ relationship suggested by Liszt (2014), the derived reddening is ~ 40 % lower.

[8] We do not include measurements of all of the H_2 fluorescent emission lines here. The general behavior is captured by the 14 lines we have featured. Note that unlike many CTTSs (e.g., France et al. 2011; Schindhelm et al. 2012), CO fluorescence is not observed in the RW Aur spectrum.

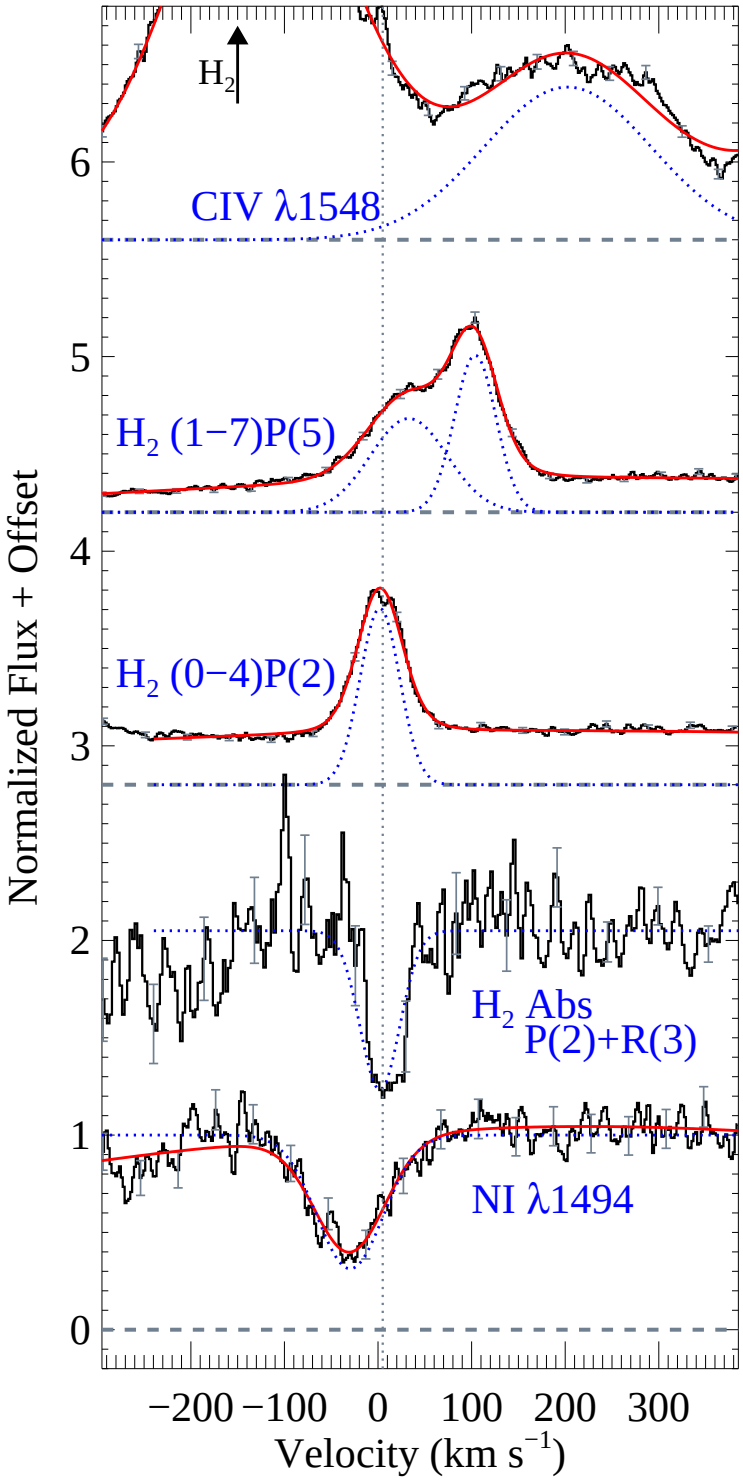

FIG. 7.— Emission and absorption profiles for species tracing all of the velocity fields in the 2013 RW Aur COS spectra (§5.1, see also Table 2). The line profiles are shown on a heliocentric velocity scale. The profiles are normalized by the maximum (average continuum) flux in a given velocity interval for emission (absorption) lines, and Gaussian fits are shown as dotted blue lines to illustrate the velocity centroids. From top, we show the red atomic lines (traced by C IV), the two-component red molecular outflow (traced by H_2 (1 – 7) P(5)), the molecular disk emission (traced by H_2 (0 – 4) P(2)) and absorption (traced by H_2 (0 – 0) P(2)), and the low-ionization blue-wind (traced by N I).

TABLE 2
RW Aur A Velocity Components and Line Widths[a].

	v_{rad} (km s^{-1})	$FWHM$ (km s^{-1})
Molecular Disk, $v \approx 0$ – $+15$ km s^{-1}		
H_2 (0 – 0) absorption lines	0 – +10	···
CO (4,2,1 – 0) absorption lines	0 – +10	···
H_2 (0 – 4)P(2) emission	+2.0 ± 0.3	50 ± 1
H_2 (0 – 5)P(2) emission	13.9 ± 1.0	45 ± 2
H_2 (4 – 1)R(17) emission	−0.8 ± 1.7	65 ± 5
H_2 (4 – 1)P(19) emission	+1.9 ± 0.7	62 ± 2
H_2 (4 – 4)R(17) emission	+2.6 ± 2.5	37 ± 6
H_2 (2 – 3)R(11) emission	+11.5 ± 0.7	48 ± 2
H_2 (2 – 6)R(11) emission	+15.7 ± 0.8	61 ± 2
H_2 (2 – 8)R(11) emission	+7.9 ± 0.8	49 ± 2
Blue Wind[b], $v \leq -30$ km s^{-1}		
Si III λ1206 absorption	−30.3 ± 0.8	292 ± 8
N I λ1243 absorption	−79.9 ± 3.3	152 ± 12
N I λ1492 absorption	−42.6 ± 1.2	100 ± 4
N I λ1494 absorption	−29.8 ± 1.3	83 ± 4
Si II λ1526 absorption	−28.9 ± 1.3	134 ± 5
Si II λ1533 absorption	−37.5 ± 1.1	155 ± 3
Red Molecular Outflow, $v \approx +40$, $+100$ km s^{-1}		
H_2 (1 – 6)P(5) emission[1]	+52.8 ± 1.1	138 ± 2
H_2 (1 – 6)P(5) emission[2]	+109.6 ± 0.5	47 ± 2
H_2 (1 – 7)R(3) emission[1]	+48.1 ± 1.1	162 ± 3
H_2 (1 – 7)R(3) emission[2]	+104.1 ± 0.5	44 ± 2
H_2 (1 – 7)P(5) emission[1]	+32.9 ± 2.0	96 ± 3
H_2 (1 – 7)P(5) emission[2]	+103.8 ± 0.6	52 ± 1
H_2 (1 – 3)R(6) emission[1]	+47.5 ± 3.9	69 ± 7
H_2 (1 – 3)R(6) emission[2]	+103.9 ± 5.0	57 ± 6
H_2 (1 – 7)R(6) emission[1]	+25.0 ± 1.5	51 ± 3
H_2 (1 – 7)R(6) emission[2]	+97.0 ± 1.0	61 ± 6
H_2 (1 – 7)P(8) emission[1]	+18.2 ± 2.2	90 ± 4
H_2 (1 – 7)P(8) emission[2]	+102.0 ± 0.8	61 ± 3
Red Atomic Emission, $v \geq +30$ km s^{-1}		
C IV λ1548 emission	+203	211
C IV λ1550 emission	+54	239
He II λ1640 emission	+90	145
O III] λ1664 emission	+39	341
N IV] λ1483 emission	+92	212
N IV] λ1486 emission	+2	367

[a] The *HST*-COS velocity scale has an accuracy of 15 km s^{-1}, the quoted velocity error bars are fitting uncertainties. The line centers and FWHMs are fit assuming a Gaussian line shape that has been convolved with the local COS line-spread-function; the centroid and line widths presented here are those of the intrinsic Gaussian emission/absorption component, prior to instrumental convolution.

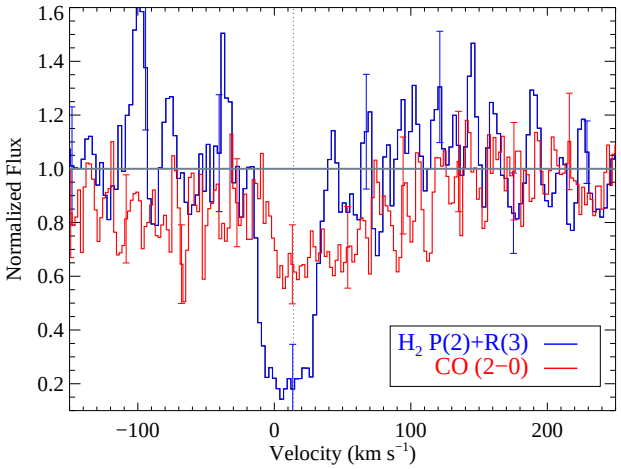

FIG. 8.— A closer look at the H_2 (blue) and CO (red) absorption velocities relative to the nominal +14 km s^{-1} stellar radial velocity of RW Aur (Hartmann et al. 1986). At the *HST*-COS resolution, multiple H_2 and CO rotational lines are blended, but the average absorption velocity is consistent with the 4.7 μm CO emission velocity v_{IR-CO} = +9.5 km s^{-1} (Brown et al. 2013).

attribute this to the molecular disk. The canonical heliocentric stellar velocity of RW Aur A is ≈ +14 km s^{-1}, and while the variable nature of the star makes this number uncertain (e.g., Hartmann et al. 1986), it agrees well with radial velocity measurements of RW Aur A (15.87 ± 0.55 km s^{-1}, but with a 5.7 km s^{-1} radial velocity centroid oscillation, Gahm et al. 1999; 15.8 km s^{-1}, Cabrit et al. 2006) and RW Aur B (15.00 ± 0.03 km s^{-1}; Nguyen et al. 2012). The molecular inner disk of RW Aur A (traced by CO fundamental emission near 4.7 μm) is blue-shifted by ≈ 7 km s^{-1} relative to the typical stellar velocity (Brown et al. 2013). Due to line-blending and the moderate-to-low S/N, it is hard to determine a precise velocity for the individual molecular absorption features in the COS spectra, however they are consistent with a centroid velocity between 0 – +10 km s^{-1} (Figure 8). We conclude that the molecular absorption species studied here are consistent with both the stellar radial velocity and the CO fundamental emission velocity. The absorbing molecular material is consistent with a disk origin, but we cannot rule out a contribution from a slow, molecular disk wind (e.g., Brown et al. 2013). However, in the slow disk wind picture (Pontoppidan et al. 2011), the wind is essentially disk material that has acquired a tangential velocity component, and is distinct from material that has been launched as an outflow from the accretion flow region. We therefore refer to the absorbing CO and H_2 gas as having a disk origin.

H_2 fluorescent progressions pumped by Lyα photons significantly redward of Lyα line-center (v_{pump} >+360 km s^{-1} from 1215.67 Å) are at similar velocities, $v_{disk}(H_2)$ = +6.8 ± 6.3 km s^{-1}, with symmetric line profiles. H_2 progressions pumped near Lyα line-center are only found in the outflows (see below). This suggests a scenario where the center of the intrinsic, broad Lyα emission profile generated near the stellar photosphere is removed through resonant scattering by neutral hydrogen atoms before these photons illuminate the disk surface. The average FWHM of the disk-origin H_2 emission lines is $\langle$FWHM$\rangle_{disk}$ = 52 ± 10 km s^{-1}, suggesting an inner H_2 disk radius (France et al. 2012b; Salyk et al. 2011) of $R_{in}(H_2) \approx 0.5$ AU (assuming $M_* = 1.2\ M_\odot$ and i = 77°). The dispersion in the disk velocities are compatible with the internal consistency of the COS wavelength solution (15 km s^{-1}; Holland et al. 2014[9]).

5.1.2. *Blue Wind and Red Molecular Outflow*

RW Aur is known to drive atomic and molecular outflows (Hirth et al. 1994; Beck et al. 2008; Melnikov et al. 2009; France et al. 2012b). We observe two outflow structures: a blue-shifted atomic absorption component and a multi-component red-shifted molecular system. The blue-shifted absorption features are low-ionization metals, with an average outflow velocity of −42 km s^{-1} (± 20 km s^{-1} standard deviation). The redshifted H_2 structures were identified by France et al. (2012b), but interestingly, earlier *HST*-GHRS observations of these lines did not show large red-shifted velocities (Ardila et al. 2002). The red-shifted H_2 fluorescence lines are exclusively pumped by Lyα photons within 100 km s^{-1} of Lyα line-center, suggesting that the pumping spectrum is a narrow Lyα profile produced by shocks within the outflow itself (Walter et al. 2003; Saucedo et al. 2003; Schneider et al. 2013). We note that the red-shifted H_2 outflow profiles observed in August 2013 have a somewhat different morphology to those seen in the first COS observations acquired in March 2011. While the earlier COS observations showed a sawtooth morphology with a steadily rising profile from roughly −10 – +100 km s^{-1}, the 2013 observations show two distinct emission components: a broad ($\langle$FWHM$\rangle_{out,broad}$ ∼ 100 km s^{-1}) component near $v_{out,broad}(H_2)$ ∼ 40 km s^{-1} and a narrow ($\langle$FWHM$\rangle_{out,narrow}$ ∼ 50 km s^{-1}) component near $v_{out,narrow}(H_2)$ ∼ 100 km s^{-1} (Figure 7, H_2 (1 – 7)P(5)). It is possible that the lower-velocity broad H_2 outflow component is associated with the +44 km s^{-1} near-IR H_2 outflow detected in RW Aur (Beck et al. 2008). Future studies of the molecular outflows from RW Aur would benefit from long-slit spectral observations.

5.1.3. *Red Atomic Emission*

Finally, we observe red-shifted emission from relatively high ionization species at a variety of velocities. The centroid velocity of C IV λ1548 is compromised by a line-blend with the red-shifted H_2 (1 – 8) R(3) line, and in general the high-ionization species displayed non-Gaussian, asymmetric line profiles. The C IV λ1550 and He II λ1640 lines are redshifted by approximately +200 km s^{-1} relative to the 2011 data described in detail by Ardila et al. (2013). The O III] λ1666 centroid has redshifted by ∼ +100 km s^{-1} relative to 2011 and the N IV] semi-forbidden lines are only detected in 2013. There is a strong, broad unidentified feature near 1472 Å that was not present in the 2011 spectra (possibly S I; Herczeg et al. 2005). The primary purpose of characterizing these velocities is to establish the origin of the molecular absorption, the evolution of the hot gas lines and far-UV continuum will be addressed in a future work.

[9] http://www.stsci.edu/hst/cos/documents/handbooks/current/cos_cover.htm

TABLE 3
RW Aur A Disk Abundance Ratios[a].

Species	$\log_{10}$N(X)	N(X)/N(H_{total})[a]
H I	$< 20.25^{+0.05}_{-0.21}$	< 0.53
H_2	$19.90^{+0.33}_{-0.22}$	> 0.24
CO	$16.1^{+0.3}_{-0.5}$	$> 3.7 \times 10^{-5}$

[a] The majority of the neutral atomic hydrogen on the RW Aur A sightline is thought to be interstellar (McJunkin et al. 2014), therefore relative abundance ratios are lower limits.
[b] N(H_{total}) = N(H I) + 2N(H_2)

5.2. *Components of the Inner Molecular Disk*

Given the numerous emitting and absorbing species attributed to the inner region of the RW Aur A disk, we will take a moment to review our best estimate for where each of these lines are being formed: The 4.7 μm CO fundamental emission (Najita et al. 2003; Brown et al. 2013) originates in the inner $\sim$ 1 AU around the star, likely with additional emission from a molecular disk wind (Pontoppidan et al. 2011). This explains the very broad line widths without pronounced double-peaked line profiles that would be expected from a purely Keplerian rotating disk. This infrared emitting CO gas is at a temperature of $\sim$ 1000 – 2000 K (Najita et al. 2003), and there is an insufficient amount of high-temperature, high-density CO beyond the emitting region to produce significant self-absorption of the CO fundamental line profiles. The narrow far-UV H_2 fluorescence emission originates in the $\sim$ 2500 K molecular disk surface between $\sim$ 0.5 – 5 AU (France et al. 2012b; Schindhelm et al. 2012b). While the emitting region may extend several scale heights above the disk surface, the lowest rovibrational levels of these fluorescent cascades do experience self-absorption (e.g., Herczeg et al. 2004). However, at the resolution of the COS observations, this is not observable in the line profiles. The H_2 emission line widths are likely dominated by rotation, but outflows may contribute to the line cores and blue wings of the observed profiles. In a strong outflow source like RW Aur A, H_2 fluorescent emission is also produced directly in the outflowing material as described in § 5.1.2.

The H_2 and CO *absorptions* that are the subject of this work originate near the surface of the inner molecular disk, but likely at lower scale heights and larger semi-major axes than the H_2 fluorescence emission from the disk. This gas is seen in absorption against the continuum emission from the accreting protostar. This absorbing molecular gas is at a temperature of a few hundred degrees K and is likely concentrated in the warm molecular surface layer from $\sim$ 2 – 10 AU. This absorbing material may also produce CO fluorescence of Lyα photons in some CTTSs (France et al. 2011a; Schindhelm et al. 2012a), but this ultraviolet CO emission is not observed towards RW Aur. We note again that this interpretation hinges upon a reasonably highly inclined disk. The measured inclination of the inner disk of RW Aur A is $i = 77^{\circ}{}^{+13}_{-15}$ (Eisner et al. 2007), however there is considerable dispersion on inclination estimates in the literature. Refined estimates of the disk inclination would be helpful to solidify the origin of the UV molecular absorption.

5.3. *The CO/H_2 Ratio and Molecular Fraction in the Disk*

Combining the kinematic, thermal, and abundance analyses presented above, we have shown that the H_2 and CO absorptions are dominated by molecular gas in the circumstellar disk around RW Aur A. The molecular abundance ratio of this material is $CO/H_2 = 1.6^{+4.7}_{-1.3} \times 10^{-4}$. This value is consistent with the canonical ratio of 10^{-4} assumed for the disk initial conditions and suggests that little chemical processing has occurred in the warm molecular surface layer of the inner disk. The inner disk CO/H_2 in RW Aur is significantly higher than the recently reported abundance ratio in the TW Hya disk, $(0.1 - 3) \times 10^{-5}$ (Favre et al. 2013). RW Aur is significantly younger than TW Hya, which may suggest a timescale for chemical evolution between 1 – 10 Myr. Favre et al. (2013) argue that the low CO abundance in the TW Hya disk is the result of CO being sequestered into hydrocarbons or CO_2 by a slow X-ray driven He^+ chemistry. Early work on the physical processes that drive this abundance evolution in the disk predict a characteristic timescale for gas phase CO reduction of $\sim 3 \times 10^6$ yr (Aikawa et al. 1997), meaning that RW Aur may not have undergone the same level of chemical processing as TW Hya. It is worth noting that the TW Hya study employed proxies for both the H_2 and CO column densities (HD (1 – 0) and $C^{18}O$ (2 – 1), respectively, although this is unlikely to impact the results significantly). Additionally, the far-IR/mm measurements are sampling gas at a few tens of degrees K in the outer disk surface, whereas the *HST* data presented here are sampling gas at several hundred degrees K that likely originates closer to the star. Finally, TW Hya is bright enough for the type of direct abundance analysis presented here, however the face-on geometry (Qi et al. 2006) is not favorable for UV disk absorption observations (see Herczeg et al. 2004).

The total line-of-sight H I column density towards RW Aur is $\log_{10}$ N(HI) = $20.25^{+0.05}_{-0.21}$ cm^{-2}, thought to be dominated by neutral hydrogen in the ISM. This value sets an upper limit to the amount of neutral hydrogen on the circumstellar line-of-sight through the disk, N_{CSM}(HI) $\leq N_{ISM}$(HI); a lower limit to the molecular fraction of the warm disk atmosphere probed by our *HST* measurements is $f_{H2} \geq 2N(H_2)$ / (N_{ISM}(HI) + $2N(H_2)$). We constrain the molecular fraction in the warm disk atmosphere of RW Aur to be $f_{H2} \geq 0.47$. This large molecular fraction is interesting because it has been suggested that circumstellar material with large molecular fractions may explain the discrepancy between optical/IR-based reddening values and N(HI)-based reddening values without having to invoke grain populations or gas-to-dust ratios that differ significantly from the diffuse and translucent ISM (McJunkin et al. 2014). Table 3 summarizes the atomic and molecular results from this work. The combination of dense cloud CO/H_2 ratio and high molecular fraction argue that the warm molecular surface layers of protoplanetary disks retain some of the physical characteristics of the dense clouds out of which they formed, at least to the $\sim$ 1 Myr age of RW Aur.

Finally, as described in the Introduction, observations of H_2 and CO UV fluorescence lines suggested high CO/H_2 ratios (0.1 – 1; e.g., France et al. 2011b;

2012). While we caution that the results presented in the present study are based on a sample size of one, they suggest that the CO/H_2 ratios derived from the emission line studies were likely misleading because of the spatial stratification of the emitting regions being studied. With a 2.5″ diameter spectroscopic aperture, *HST*-COS emission line observations sample the entire inner disk surface ($r \lesssim 200$ AU), where disk surface temperatures change from a few thousands to a few tens of degrees. The combination of the derived rotational excitation temperatures and analyses of the rotationally broadened line widths argue that the $T_{rot}(H_2) \sim 2500$ K gas originates inside 3 AU, while the cooler fluorescent CO emission originates between 2 – 10 AU (Schindhelm et al. 2012a; France et al. 2012b). These regions are spatially unresolved by COS, so while the local column densities derived for each component are robust, the columns refer to different populations of gas and therefore the inferred local CO/H_2 ratio from spatially unresolved UV fluorescence observations is not meaningful.

The UV fluorescent picture of the inner disk appears to be the following: the hot H_2-emitting population has too little CO associated with it to be detectable and the warm CO-emitting population is too cold for Lyα fluorescence of H_2 to operate efficiently. The new H_2 and CO absorption line spectra presented in this work overcome these geometric complications by sampling material on a single pencil-beam sightline to the central star. The similarity of the CO and H_2 excitation temperatures and velocity structure argue for a common spatial origin, with a CO/H_2 abundance ratio of CO/$H_2 \approx 1.6 \times 10^{-4}$.

6. SUMMARY

We have presented new contemporaneous measurements of CO and H_2 absorption through the "warm molecular layer" in the protoplanetary disk around the Classical T Tauri Star RW Aurigae A. We have demonstrated the use of a newly commissioned observing mode of the *Hubble Space Telescope* to detect warm H_2 in this region for the first time. Spectral analyses of these data reveal the following major findings:

1. The spectra are composed of emission from the accretion region near the stellar photosphere, the molecular disk, and several outflow components. The relative spatial distribution of these components can be inferred from their velocities.

2. Absorption spectra from H_2 and CO are observed and are consistent with an origin in the upper layers of the RW Aur circumstellar disk. A low-ionization, low-velocity atomic outflow is also detected in absorption.

3. Spectral synthesis modeling indicates that the molecular absorbers arise in a common parcel of disk gas, characterized by $\log_{10}$ N(H_2) = $19.90^{+0.33}_{-0.22}$ cm^{-2} at $T_{rot}(H_2) = 440 \pm 39$ K, with a molecular fraction $f_{H2} \geq 0.47$. The CO component has $\log_{10}$ N(CO) = $16.1^{+0.3}_{-0.5}$ cm^{-2} at T_{rot}(CO) = 200^{+650}_{-125} K.

4. We derive an abundance ratio of CO/H_2 = $1.6^{+4.7}_{-1.3} \times 10^{-4}$ for the inner disk gas, consistent with canonical interstellar dense cloud value.

The data presented here were obtained through *HST* Guest Observing program 12876. Initial design and characterization of the COS G130M λ1222 mode was performed as part of *HST* Guest Observing program 12505. We appreciate helpful discussions with Eric Burgh, Eric Schindhelm, and Christian Schneider during the course of this work. This work was partially supported by NASA grant NNX08AC146 to the University of Colorado at Boulder and KF acknowledges support from a Nancy Grace Roman Fellowship during a portion of this work.

REFERENCES

Aikawa, Y., Umebayashi, T., Nakano, T., & Miyama, S. M. 1997, ApJ, 486, L51
Andrews, S. M. & Williams, J. P. 2005, ApJ, 631, 1134
Ardila, D. R., Basri, G., Walter, F. M., Valenti, J. A., & Johns-Krull, C. M. 2002, ApJ, 566, 1100
Ardila, D. R., Herczeg, G. J., Gregory, S. G., et al., 2013, ApJS, 207, 1
Armitage, P. J. 2007, ApJ, 665, 1381
Armitage, P. J., Livio, M., Lubow, S. H., & Pringle, J. E. 2002, MNRAS, 334, 248
Bary, J. S., Weintraub, D. A., Shukla, S. J., Leisenring, J. M., & Kastner, J. H. 2008, ApJ, 678, 1088
Beck, T. L., McGregor, P. J., Takami, M., & Pyo, T.-S. 2008, ApJ, 676, 472
Bergin, E. A., Cleeves, L. I., Gorti, U., et al., 2013, Nature, 493, 644
Bohlin, R. C., Savage, B. D., & Drake, J. F. 1978, ApJ, 224, 132
Bond, J. C., O'Brien, D. P., & Lauretta, D. S. 2010, ApJ, 715, 1050
Brown, J. M., Pontoppidan, K. M., van Dishoeck, E. F., et al., 2013, ApJ, 770, 94
Bruderer, S. 2013, A&A, 559, A46
Burgh, E. B., France, K., & McCandliss, S. R. 2007, ApJ, 658, 446
Cabrit, S., Pety, J., Pesenti, N., & Dougados, C. 2006, A&A, 452, 897
Carmona, A., van den Ancker, M. E., Henning, T., et al., 2008, A&A, 477, 839
Carruthers, G. R. 1970, ApJ, 161, L81
Danforth, C. W., Keeney, B. A., Stocke, J. T., Shull, J. M., & Yao, Y. 2010, ApJ, 720, 976
Diplas, A. & Savage, B. D. 1994, ApJS, 93, 211
Duchêne, G., Monin, J.-L., Bouvier, J., & Ménard, F. 1999, A&A, 351, 954
Dullemond, C. P., Hollenbach, D., Kamp, I., & D'Alessio, P. 2007, Protostars and Planets V, 555
Eidelsberg, M., Jolly, A., Lemaire, J. L., Tchang-Brillet, W.-Ü., Breton, J., & Rostas, F. 1999, A&A, 346, 705
Eidelsberg, M. & Rostas, F. 2003, ApJS, 145, 89
Eisner, J. A., Hillenbrand, L. A., White, R. J., et al., 2007, ApJ, 669, 1072
Elias, J. H. 1978, ApJ, 224, 857
Fang, M., Kim, J. S., van Boekel, R., et al., 2013, ApJS, 207, 5
Favre, C., Cleeves, L. I., Bergin, E. A., Qi, C., & Blake, G. A. 2013, ApJ, 776, L38
Fedele, D., van den Ancker, M. E., Henning, T., Jayawardhana, R., & Oliveira, J. M. 2010, A&A, 510, A72
Federman, S. R., Glassgold, A. E., Jenkins, E. B., & Shaya, E. J. 1980, ApJ, 242, 545
France, K., Burgh, E. B., Herczeg, G. J., et al., 2012a, ApJ, 744, 22
France, K., Schindhelm, E., Bergin, E. A., Roueff, E., & Abgrall, H. 2014, ApJ, 784, 127
France, K., Schindhelm, E., Burgh, E. B., et al., 2011a, ApJ, 734, 31

France, K., Schindhelm, E., Herczeg, G. J., et al., 2012b, ApJ, 756, 171
France, K., Yang, H., & Linsky, J. L. 2011b, ApJ, 729, 7
Gahm, G. F., Petrov, P. P., Duemmler, R., Gameiro, J. F., & Lago, M. T. V. T. 1999, A&A, 352, L95
Glassgold, A. E., Najita, J., & Igea, J. 2004, ApJ, 615, 972
Green, J. C., Froning, C. S., Osterman, S., et al., 2012, ApJ, 744, 60
Haridass, C. & Huber, K. P. 1994, ApJ, 420, 433
Hartigan, P., Edwards, S., & Ghandour, L. 1995, ApJ, 452, 736
Hartigan, P. & Hillenbrand, L. 2009, ApJ, 705, 1388
Hartmann, L., Hewett, R., Stahler, S., & Mathieu, R. D. 1986, ApJ, 309, 275
Hayashi, C., Nakazawa, K., & Nakagawa, Y. 1985, in Protostars and planets II (A86-12626 03-90). Tucson, AZ, University of Arizona Press, 1985, p. 1100-1153., ed. D. C. Black & M. S. Matthews, 1100–1153
Herczeg, G. J. & Hillenbrand, L. A. 2014, ApJ, 786, 97
Herczeg, G. J., Walter, F. M., Linsky, J. L., et al., 2005, AJ, 129, 2777
Herczeg, G. J., Wood, B. E., Linsky, J. L., Valenti, J. A., & Johns-Krull, C. M. 2004, ApJ, 607, 369
Hernández, J., Hartmann, L., Megeath, T., et al., 2007, ApJ, 662, 1067
Hirth, G. A., Mundt, R., Solf, J., & Ray, T. P. 1994, ApJ, 427, L99
Ida, S. & Lin, D. N. C. 2004, ApJ, 604, 388
Ingleby, L., Calvet, N., Herczeg, G., et al., 2013, ApJ, 767, 112
Ingleby, L., Calvet, N., Hernández, J., et al., 2011a, AJ, 141, 127
—. 2011b, AJ, 141, 127
Jayawardhana, R., Coffey, J., Scholz, A., Brandeker, A., & van Kerkwijk, M. H. 2006, ApJ, 648, 1206
Kenyon, S. J. & Hartmann, L. 1995, ApJS, 101, 117
Kriss, G. A. 2011, Improved Medium Resolution Line Spread Functions for COS FUV Spectra, Tech. rep.
Lacy, J. H., Knacke, R., Geballe, T. R., & Tokunaga, A. T. 1994, ApJ, 428, L69
Lahuis, F., van Dishoeck, E. F., Blake, G. A., et al., 2007, ApJ, 665, 492
Liszt, H. 2014, ApJ, 780, 10
Mandy, M. E. & Martin, P. G. 1993, ApJS, 86, 199
Markwardt, C. B. 2009, in Astronomical Society of the Pacific Conference Series, Vol. 411, Astronomical Data Analysis Software and Systems XVIII, ed. D. A. Bohlender, D. Durand, & P. Dowler, 251
Martin-Zaïdi, C., Augereau, J.-C., et al., 2010, A&A, 516, A110
Martin-Zaïdi, C., Deleuil, M., Le Bourlot, J., et al., 2008, A&A, 484, 225
McCandliss, S. R. 2003, PASP, 115, 651
McCandliss, S. R., France, K., Osterman, S., et al., 2010, ApJ, 709, L183
McJunkin, M., France, K., Burgh, E. B., et al., 2013, ApJ, 766, 12
McJunkin, M., France, K., Schneider, P. C., et al., 2014, ApJ, 780, 150
Meijerink, R., Aresu, G., Kamp, I., et al., 2012, A&A, 547, A68
Melnikov, S. Y., Eislöffel, J., Bacciotti, F., Woitas, J., & Ray, T. P. 2009, A&A, 506, 763
Mordasini, C., Alibert, Y., & Benz, W. 2009, A&A, 501, 1139
Najita, J., Carr, J. S., & Mathieu, R. D. 2003, ApJ, 589, 931
Najita, J. R., Carr, J. S., Glassgold, A. E., & Valenti, J. A. 2007, Protostars and Planets V, 507
Nguyen, D. C., Brandeker, A., van Kerkwijk, M. H., & Jayawardhana, R. 2012, ApJ, 745, 119
Öberg, K. I., Murray-Clay, R., & Bergin, E. A. 2011, ApJ, 743, L16
Pascucci, I., Gorti, U., Hollenbach, D., et al., 2006, ApJ, 651, 1177
Penton, S. V., Aloisi, A., Bostroem, K. A., et al., 2013, in American Astronomical Society Meeting Abstracts, Vol. 221, American Astronomical Society Meeting Abstracts, #344.04
Penton, S. V., Osterman, S. N., France, K., Oliveira, C., & Sahnow, D. J. 2012, in American Astronomical Society Meeting Abstracts, Vol. 219, American Astronomical Society Meeting Abstracts #219, #241.19
Pontoppidan, K. M., Blake, G. A., & Smette, A. 2011, ApJ, 733, 84
Qi, C., Wilner, D. J., Calvet, N., et al., 2006, ApJ, 636, L157
Rachford, B. L., Snow, T. P., Tumlinson, J., et al., 2002, ApJ, 577, 221
Richter, M. J., Jaffe, D. T., Blake, G. A., & Lacy, J. H. 2002, ApJ, 572, L161
Roberge, A., Lecavelier des Etangs, A., Grady, C. A.,et al., 2001, ApJ, 551, L97
Salyk, C., Blake, G. A., Boogert, A. C. A., & Brown, J. M. 2009, ApJ, 699, 330
Salyk, C., Pontoppidan, K. M., Blake, G. A., Najita, J. R., & Carr, J. S. 2011, ApJ, 731, 130
Saucedo, J., Calvet, N., Hartmann, L., & Raymond, J. 2003, ApJ, 591, 275
Savage, B. D., Bohlin, R. C., Drake, J. F., & Budich, W. 1977, ApJ, 216, 291
Schindhelm, E., France, K., Burgh, et al., 2012a, ApJ, 746, 97
Schindhelm, E., France, K., Herczeg, G. J., et al., 2012b, ApJ, 756, L23
Schneider, P. C., Eislöffel, J., Güdel, M., et al., 2013, A&A, 557, A110
Sheffer, Y., Rogers, M., Federman, S. R., et al., 2008, ApJ, 687, 1075
Sicilia-Aguilar, A., Hartmann, L. W., Hernández, J., Briceño, C., & Calvet, N. 2005, AJ, 130, 188
Thi, W.-F., van Zadelhoff, G.-J., & van Dishoeck, E. F. 2004, A&A, 425, 955
Torres, R. M., Loinard, L., Mioduszewski, A. J., & Rodríguez, L. F. 2007, ApJ, 671, 1813
Trilling, D. E., Lunine, J. I., & Benz, W. 2002, A&A, 394, 241
Visser, R., Doty, S. D., & van Dishoeck, E. F. 2011, A&A, 534, A132
Walter, F. M., Herczeg, G., Brown, A.,et al., 2003, AJ, 126, 3076
Ward, W. R. 1997, Icarus, 126, 261
White, R. J. & Ghez, A. M. 2001, ApJ, 556, 265
Woitas, J., Leinert, C., & Köhler, R. 2001, A&A, 376, 982
Woitas, J., Ray, T. P., Bacciotti, F., Davis, C. J., & Eislöffel, J. 2002, ApJ, 580, 336
Woitke, P., Dent, B., Thi, W., et al., 2009, in American Institute of Physics Conference Series, Vol. 1094, American Institute of Physics Conference Series, ed. E. Stempels, 225–233
Yang, H., Linsky, J. L., & France, K. 2011, ApJ, 730, L10+